

Estimation of Frequency Dispersive Complex Permittivity Seen by Each Antenna for Enhanced Multistatic Radar Medical Imaging

A. Zamani, *Student Member, IEEE*, A.M. Abbosh, *Senior Member, IEEE*

Abstract—Radar-based microwave imaging requires the effective dielectric properties of the imaged object as a priori information. A technique to determine the effective complex permittivity seen by each imaging antenna across the used frequency band of a multistatic imaging domain is presented. The method uses spatial statistical techniques to model the complex permittivity of the imaging domain as a function of scattering parameters. The proposed method does not require any predefined gap between the antennas and the imaged object, nor does it need the imaged object to be centered within the imaging domain. Also, the method does not need to know boundaries of the imaged object. The proposed method is tested via simulations and experiments using a multistatic human torso imaging system. The collected data across the band 0.65-1.75 GHz using twelve antennas around the human torso are processed to generate accurate images. The results demonstrate significant improvements in image quality and detection accuracy compared to conventional average-permittivity methods. The efficacy of the proposed method is verified experimentally in detecting an early case of lung cancer in a human torso phantom.

Index Terms—Microwave imaging, multistatic radar imaging, torso imaging, lung cancer.

I. INTRODUCTION

Ultra-wideband radar technique is a well-established approach that is being investigated for microwave medical imaging [1]-[8]. The contrast in the dielectric properties between healthy and unhealthy tissues at microwave frequencies enables the use of that technique for a range of medical applications, such as the detection of breast cancer [1]-[4], lung cancer [7], and brain stroke [8].

Various radar imaging techniques, such as delay-and-sum [1], space-time beamforming [2]-[3] and fast frequency domain [8] algorithms, have been established for medical imaging applications. All of those algorithms need a priori information on the wave's propagation speed in the imaging domain. Thus, the effective dielectric constant of the domain is typically assumed in the homogeneous propagation models employed by those algorithms. However, due to the multiple reflection and refraction of the electromagnetic wave in a dispersive and heterogeneous environment, such as the human torso, the wave passes through different tissues and follows different paths depending on the transmitter-receiver location with respect to the imaged object. Therefore, each transmitting-receiving

antenna pair “sees” different effective permittivity, which is the average permittivity of tissues and space through which the electromagnetic wave propagates for a specific transmitter-receiver scenario. That effective permittivity thus depends on the location of the antennas with respect to the imaging domain in addition to properties of the imaged object and its location with respect to those antennas. Therefore, a method to accurately predict the location-specific dielectric properties of the imaged domain is required for successful radar-based imaging algorithms.

Different methods to estimate the permittivity of the imaging domain were proposed [9]-[11]. In those methods, the time delay between two sets of measurements (with and without the imaging subject or with its metallic equivalent) are compared to determine the average permittivity of the subject. In [12], Multiple Signal Classification (MUSIC) technique was used to calculate the Time-of-Flight (ToF) of the signals through the imaged domain to estimate the average dielectric permittivity of the imaged object. Those techniques gave promising results for low-loss, frequency-independent and homogeneous objects. However, the heterogeneous objects with frequency dispersive properties, like human tissues, can lead to inaccurate ToF estimation [13] which subsequently result in inaccurate images. With the heterogeneous structure of human organs, which creates multiple signal paths and possible surface waves, the exact value and meaning of ToF are quite ambiguous.

In [14], the dielectric constant of the imaged subject is modeled as a function of antenna's position and imaged location within the imaging domain of a monostatic imaging system. The used dielectric model is specific to the imaged object and is thus highly sensitive to variations in the size and shape of that object. In addition, the location of the imaged object with respect to the antennas should be known and agree with a pre-defined value for an accurate estimation. In another approach, the most likely effective permittivity of the imaging domain is estimated by optimizing the image quality [15], [16]. Those works showed interesting results for monostatic head and breast imaging. However, they are time consuming if used in multistatic configurations with large imaging domains. In addition, they may converge on local maxima (ghost targets) in highly heterogeneous environments, causing inaccurate detection as they rely on finding one effective permittivity for the whole domain. In [17]-[18], the relative permittivity of biological tissues is expressed as a weighted sum of scattering parameters to determine the electrical properties of deep internal organs for monitoring purposes. However, that method needs the average permittivity and imaged object's borders as a

Manuscript submitted November 25, 2016.

The authors are with School of Information Technology and Electrical Engineering, University of Queensland, St Lucia, 4072, Brisbane, Australia
Email: a.zamani@uq.edu.au

priori information to reduce the training matrix size. In addition, the measurements are performed in a low frequency step for a two-layer structure, which is not applicable for ultra-wideband imaging techniques that deal with heterogeneous frequency dispersive tissues.

A method to estimate the complex permittivity of the imaging domain using a statistical modeling technique is presented. It has the capability to accurately predict the effective complex permittivity seen by any imaging antennas across the whole used band. The proposed method does not require any predefined distance between the antennas and the imaged object, nor does it need the imaged object to be centered within the imaging domain. Also, the method does not need to know boundaries of the imaged object. Those three parameters are quite important in medical applications, where the distance between the antennas and the imaged object, which may have any shape or size, cannot be fully controlled or known. The performance of the proposed method is successfully verified by realistic simulations and validated by experiments on a human torso phantom with the aim to detect early lung cancer.

II. PROPOSED METHOD

Assume that an imaging domain is surrounded by N_a antennas operating in a multistatic mode as shown in Fig. 1. The effective permittivity of the imaging domain seen by any antenna depends on properties, size and shape of the imaged object located in the domain. For a heterogeneous object with frequency dispersive properties, the effective permittivity seen by an antenna depends also on the location of that antenna with respect to the object and the used frequency. Thus, the assumption of one effective permittivity, or even the prediction of one effective value when using radar beamforming processing techniques does not really enable accurate imaging. Thus, a method that can predict the effective permittivity seen by any antenna is a must for accurate imaging.

The effective permittivity can be expressed as a function of the scattering parameters. So, if a set of S-parameters are calculated for a specific imaging domain (i.e. specific antennas and array structure) with known properties, these parameters can be used to train the system to predict the effective complex permittivity when imaging an unknown object. In the work [17], such a function was solved using the ordinary least squares linear regression methods in a bi-static configuration. However, due to the large number of variables (S-parameters)

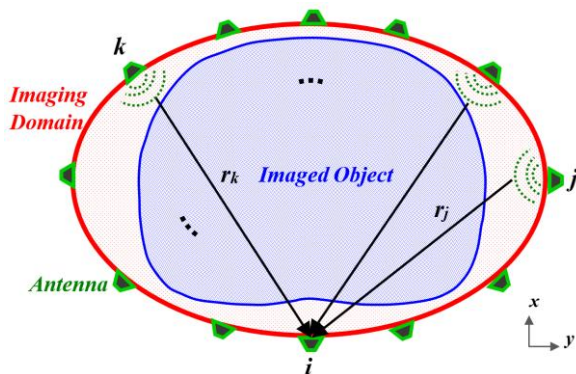


Fig. 1. The used imaging domain.

in the adopted multistatic configuration, such a function leads to ill-posed problems, where more than one weighting factor satisfy the linear equation, leading to over or underdetermined equations.

To address this issue, additional information must be introduced to the ill-posed problem to prevent over- or under-fitting. To that end, the problem is regularized by the spatial regionalization of the scattering parameters. Thus, the variogram [19], which describes the degree of spatial dependence of signals, is calculated for each receiver i :

$$\gamma_i(h) = \frac{1}{2|N(h)|} \sum_{(j,k) \in N(h)} |S_{ij} - S_{ik}|^2 \quad (1)$$

where, h is the distance between the j th and k th transmitting antenna locations, S_{ij} is the received signal at i th antenna transmitted from j th antenna using N_f frequency samples, and $N(h)$ denotes the set of pairs of observations ij and ik such that $|r_{ij} - r_{ik}| = h$ and $|N(h)|$ is the number of pairs in the set. Low values of h represent neighboring antennas, which receive highly correlated signals, and thus their corresponding γ is low, whereas antennas that are distant from each other (high values of h) deliver high values of γ . By using (1), each receiver in the multistatic configuration is presented by a function $\gamma(h)$. Therefore, $0.5 \times N_a \times (N_a + 1)$ independent variables/signals are reduced to N_a regularized functions that incorporate the spatial features of relevant signals.

To link $\gamma(h)$ with the dielectric properties of the imaging domain, the effective permittivity from the view point of i th receiver ε_i is modeled as

$$\varepsilon_i = \mathbf{f}(s)\mathbf{w} + z(s) \quad (2)$$

where $s = \{\gamma, h\}$ is the function's input in which γ is calculated using (1), $\mathbf{f}(s) = [1, \gamma, h, \gamma^2, \gamma h, h\gamma, h^2]$ is a vector of quadratic regression function, and \mathbf{w} is the 7×1 vector of regression coefficients to be calculated for a minimized error $z(s)$. There are N_h functions of ε_i for h values extending from 0 to the length of the maximum axis of the elliptical antenna array. Those quadratic functions relate discrete values of γ to h and to ε . To obtain the best unbiased estimation of \mathbf{w} , it is necessary to train the model using training samples, which are generated using the calculated S-parameters of the imaging domain when filled with uniform media that have certain assumed permittivity values (sample mediums). In that regard, the imaging domain (such as the ellipse in Fig. 1) is assumed to have N_ε different permittivity values ε_n ($n = 1$ to N_ε) and the corresponding multistatic S-parameters are calculated at each assumption. The calculated S-parameters are then used in (1) to obtain $\gamma(h)$ and thus the corresponding training functions $s_n = \{\gamma_n, h_n\}$ ($n = 1$ to N_ε) and $\mathbf{f}(s_n)$. Assuming N_ε different training samples with assumed permittivity values ε_n ($n = 1$ to N_ε), (2) can be written in a matrix form as

$$\boldsymbol{\varepsilon}_i = \mathbf{F}\mathbf{w} + \mathbf{z} \quad (3)$$

where $\boldsymbol{\varepsilon}_i = [\varepsilon_1, \dots, \varepsilon_M]^T$ is the vector of permittivity with the dimension of $M (= N_\varepsilon \times N_h) \times 1$, $\mathbf{F} = [\mathbf{f}(s_1), \dots, \mathbf{f}(s_M)]^T$ is the $M \times 7$ regression function matrix and $\mathbf{z} = [z(s_1), \dots, z(s_M)]^T$ is the $M \times 1$ error vector. The matrix of coefficients estimator $\hat{\mathbf{w}}$ (the

notation $\hat{\cdot}$ represents the estimated coefficient) can be determined subject to the minimization of the total sum of squares (TSS) of the error, \mathbf{z}

$$TSS = \sum_{n=1}^M |z(s_n)|^2 = (\boldsymbol{\varepsilon} - \mathbf{F}\mathbf{w})^T (\boldsymbol{\varepsilon} - \mathbf{F}\mathbf{w}) \quad (4)$$

The generalized least squares solution of \mathbf{w} is then [20]

$$\hat{\mathbf{w}} = (\mathbf{F}^T \mathbf{C}^{-1} \mathbf{F})^{-1} \mathbf{F}^T \mathbf{C}^{-1} \boldsymbol{\varepsilon} \quad (5)$$

In this equation, $\mathbf{C} = [c_{ij}]$ is an $M \times M$ stochastic-process correlation matrix with $c_{ij} = \rho(s_i, s_j)$, $i, j = 1, \dots, M$, where ρ is the correlation function between the permittivity values at samples $s_i = \{\gamma_i, h_i\}$, $s_j = \{\gamma_j, h_j\}$. After testing different correlation functions, such as linear [21], Gaussian [22] and exponential functions [23], the latter is selected as it gives the best fit to the data.

After finding $\hat{\mathbf{w}}$ for the designed imaging domain (antenna array and its structure), the training step finishes and the system is ready to be used to image an unknown object of any shape and size as long as it fits within that domain. In this case the permittivity value $\hat{\varepsilon}_i$ for the measured S-parameters in the presence of an unknown imaged object with $s = \{\gamma, h\}$ is approximated by [24]

$$\hat{\varepsilon}_i(s) = \mathbf{f}(s)\hat{\mathbf{w}} + \mathbf{c}(s)^T \mathbf{C}^{-1} (\boldsymbol{\varepsilon} - \mathbf{F}\hat{\mathbf{w}}) \quad (6)$$

where, $\mathbf{c}(s)$ is the correlation matrix between the input s from the unknown object and the training samples. Finally, the observed effective permittivity by the i th antenna is calculated by averaging the permittivity values over all values of h :

$$\hat{\varepsilon}_i^{effective} = \frac{1}{|N_h|} \sum_{j=1}^{N_h} \hat{\varepsilon}_i(s_j) \quad (7)$$

In summary, the proposed method can be represented by the flowchart shown in Fig. 2 and explained by the following steps:

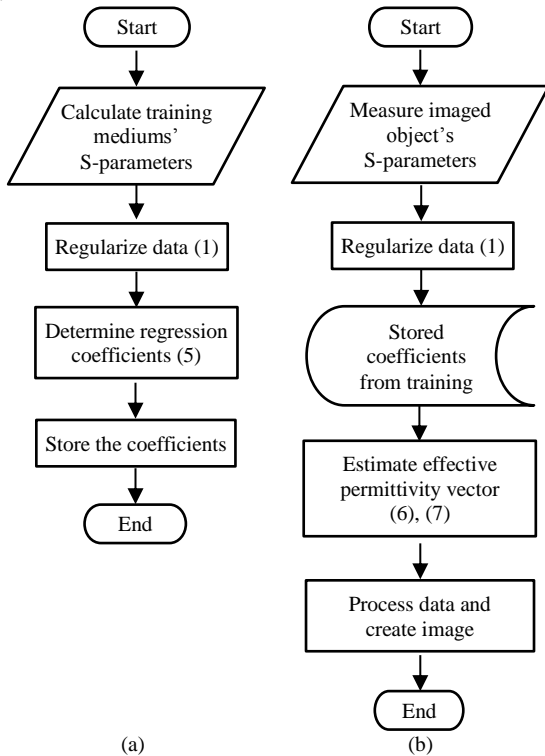


Fig. 2. Flowchart of the proposed method, (a) training and (b) imaging.

- a) Training;
 1. Calculate the multistatic frequency domain S-parameters for certain range of training mediums,
 2. Regularize the S-parameters using (1),
 3. Determine the vector of the coefficients estimator $\hat{\mathbf{w}}$, using (5),
- b) Imaging;
 1. Insert the object to be imaged in the imaging domain and collect the multistatic frequency domain S-parameters with the existence of the unknown imaged object,
 2. Regularize the measured S-parameters using (1),
 3. Estimate the effective complex permittivity vector using (6) and (7).
 4. Construct an image using the estimated permittivity values and proper imaging algorithm.

III. VERIFICATION

To verify the proposed method in medical applications, a realistic simulation environment for human torso imaging is established in ANSYS HFSS. An elliptical shaped antenna array is utilized to simulate a realistic scenario in which the distance between the antennas and the imaged object, such as the human torso, is not uniform (Fig. 3). The used antenna array consists of compact unidirectional ultra-wideband antennas [25]. A photo of the used antenna and its performance are depicted in Fig. 4. The utilized antenna has the dimensions of $100 \times 120 \times 0.8 \text{ mm}^3$ and operates across the band 0.65-1.75 GHz with more than 10 dB return loss in free space and more than 20 dB mutual coupling between any two neighboring antennas of the array. In the training and imaging steps, a signal covering the frequency band 0.65-1.75 GHz at

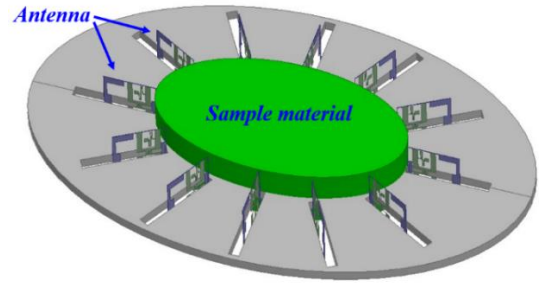


Fig. 3. Training setup.

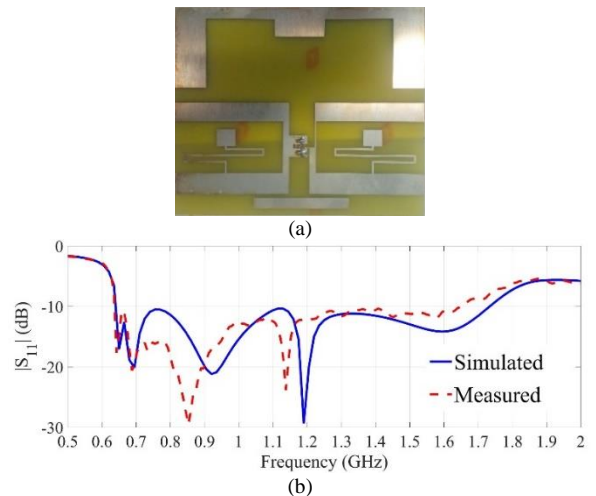


Fig. 4. (a) The utilized antenna [25], and (b) its reflection coefficient.

10 MHz intervals is sequentially transmitted by one antenna, while all of the antennas receive the scattered signals, which are recorded for further processing.

The required number of antennas for the proposed method is calculated by the degree of freedom (DOF) theory [26]. According to DOF, the imaging domain's perimeter should be sampled at a rate equal to one half of the wavelength λ in air to get enough information from the inside of the imaging object:

$$\Delta\phi = \lambda/(2a) \quad (8)$$

wherein, a is the radius of the imaging object. In this case, the number of DOF of the torso imaging system, and thus the minimum number of antennas required to collect the available information at the highest frequency is $2ka = 12$. To investigate the effect of the number of antennas on the estimation accuracy, the estimation error for different number of antennas is calculated and plotted in Fig. 5. It can be seen from Fig. 5 that the estimation error decreases with the increase in the number of imaging antennas. However, there is no significant improvement in the estimation error when increasing the number of antennas to more than 12. This issue can be explained by the fact that increasing the number of antenna significantly means that neighboring antennas get closer to each other and they start to "see" the same effective permittivity from the imaged domain. Assuming 5% as an acceptable estimation error for the permittivity and conductivity [11], [17], at least 12 antennas are required to estimate those values in the considered torso imaging domain. In the training step, no object is inserted in the imaging domain. Instead, a uniform training medium with the height equal or more than the height of the antennas fills the whole imaging domain, while the dielectric properties of air is chosen for the medium around and behind the antennas. The number of training media, or samples (M), needed to train the method affects the estimation accuracy. Essentially, larger number of training samples means more accurate estimation of the permittivity, but at the expense of longer time for data gathering and model training. To determine a suitable number of samples, a design space including all possible combinations of permittivity and conductivity values is considered. Since the aim of this work is torso imaging, the design space is sampled using the ranges of $\epsilon_r = [1, 63]$ and $\sigma = [0, 1.9]$ to cover all the permittivity values of human torso tissues. The time needed for recording the required data in simulations and training using three different permittivity and conductivity sampling intervals ($\Delta\epsilon_r, \Delta\sigma$) is provided in Table I. The computations are

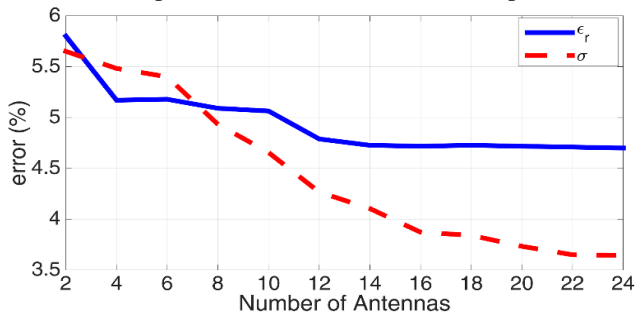


Fig. 5. Estimation error with number of antennas.

TABLE I
COMPUTATION TIME FOR DIFFERENT NUMBER OF SAMPLES

$[\Delta\epsilon_r, \Delta\sigma]$	[5, 0.5]	[2, 0.2]	[1, 0.1]
Number of samples (M)	65	315	1260
Time for gathering data (h)	260	1260	5040
Time for training (s)	164	3116	263520

performed by a 3.4 GHz and 16 GB RAM personal computer. The time for data gathering is calculated by multiplying the number of simulations (M) in the required time for one simulation run (≈ 4 hours). It is clear from Table I that 5040 hours (7 months) is needed to achieve perfectly accurate model. It is also clear that the required time to train the model dramatically increases with the increase in the number of samples.

To find a suitable compromise between the high gathering and training time needed with large number of samples and estimation accuracy, the estimation errors for different sampling intervals are calculated based on Monte Carlo sensitivity analysis [27]. In that regard, one fixed value for each parameter (e.g. conductivity) is randomly selected within its range, while the other parameter (e.g. permittivity) is sampled at different intervals. The relevant S-parameters are then calculated when the imaging domain is filled with the sampled permittivity values. The obtained S-parameters are used in (1) to regularize the data, and the estimation error $z(s)$ is calculated using (4), where \mathbf{w} is replaced by $\hat{\mathbf{w}}$. The estimation errors for different sampling intervals are plotted in Fig. 6 (a) and (b), respectively. It is clear from Fig. 6 that the error between the estimated and actual values of permittivity and conductivity increases by increasing the sampling intervals. According to Fig. 6, the maximum sampling intervals for the permittivity and conductivity are $\Delta\epsilon_r = 2$ and $\Delta\sigma = 0.2$, respectively, to achieve less than 5% estimation error. Therefore, 315 training samples are required to fill the design space with $\Delta\epsilon_r = 2$ and $\Delta\sigma = 0.2$ sampling intervals. Fig. 7 (a) shows distribution of the

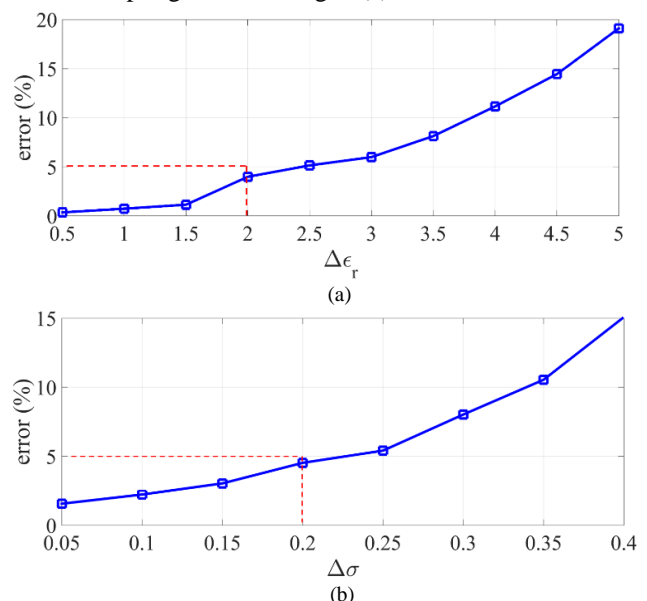


Fig. 6. Estimation error against sampling size, for (a) relative permittivity and (b) conductivity.

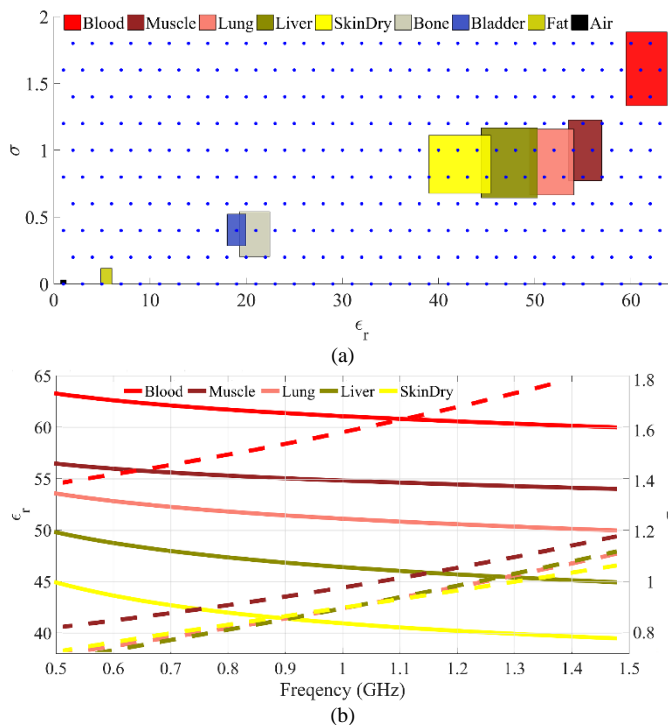


Fig. 7. (a) Dielectric properties of the training samples along with the ranges of variations for dielectric parameters of human torso tissues (colored boxes), and (b) variation of relative permittivity (solid lines) and conductivity (dash lines) with frequency.

complex permittivity values of the selected samples (blue dots) along with the range of values for the dielectric parameters of different human torso tissues (colored boxes). Variations of those parameters for some of the torso tissues with frequency are also shown in Fig. 7 (b).

The calculated S-parameters for all of the training media are used to model the dielectric properties of the imaging domain using (1) – (5). Once the model is created, it can be used to estimate the dielectric properties of any imaged object using (7). While this model is exclusive to the trained imaging domain, i.e. the antenna array and size of the imaging domain, it is valid for imaging any object located within that domain.

A. Simulations

The system is used to image a three-dimensional human torso model (EMAG model) including all of the torso tissues with their realistic dispersive properties (Fig. 7). The torso model and a multistatic antenna array are integrated with a multistatic frequency-based radar imaging algorithm to form a microwave torso imaging system (Fig. 8). To emulate the scenario of lung cancer patient, a 1 cm radius sphere of tissue with tumor properties is inserted inside one of the lungs.

The simulation is conducted in CST and the recorded S-parameters are regularized by (1). The regularized signals are then used for estimating the effective permittivity of the imaging domain by the obtained model in training using (6) and (7). The simulations are conducted for healthy (without tumor) and unhealthy (with tumor) cases to show effect of the change in the dielectric properties of the tissues in the estimation of the effective permittivity. The estimated relative permittivity and conductivity of the imaging domain at the center frequency

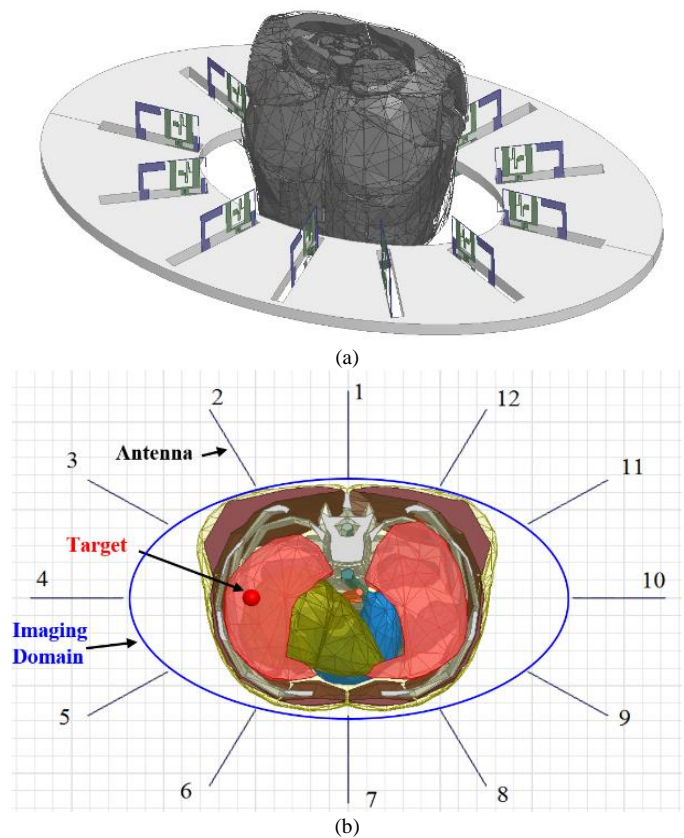


Fig. 8. Simulation setup to image an object (human torso), (a) side view and (b) cross-section up view.

(1 GHz) from each antenna perspective are depicted in Fig. 9 for both healthy and unhealthy cases. Their values for antennas 1 and 4 over the used frequency band are also shown in Fig. 10.

As it is clear from Fig. 9, the estimated permittivity and conductivity values of the unhealthy case is slightly larger than the values for the healthy one due to the presence of a small tumor with high dielectric constant in the unhealthy case. Of course, the slight difference in those values between healthy and unhealthy cases cannot be interpreted directly from Figs. 9-10 to say whether a case is healthy or not. An efficient processing algorithm is still needed to create a clear image that enables accurate diagnosis. The target from those figures is to show that the proposed method is quite sensitive even to a very small variation in the effective permittivity due to a small abnormality, which means better diagnosis using the proposed method in combination with proper processing techniques. That difference is more evident in the antennas that are close to the tumor location, especially antenna 4. Most importantly, the dielectric properties from the view point of those antennas are lower than the observed values from the other antennas' perspective due to the larger air gap between antennas 4 and 10 and the torso. On the other hand, the antennas that are close to the torso, such as antennas 1, 2, 12, 6, 7 and 8, see the highest effective permittivity and conductivity. By using antenna-specific permittivity values in a radar-based imaging algorithm, the imaging results are expected to be more accurate and there is no need to adjust the distance between the antennas and the imaged object to be uniform.

Fig. 10 demonstrates that the proposed method can estimate the complex permittivity of the dispersive imaging domain.

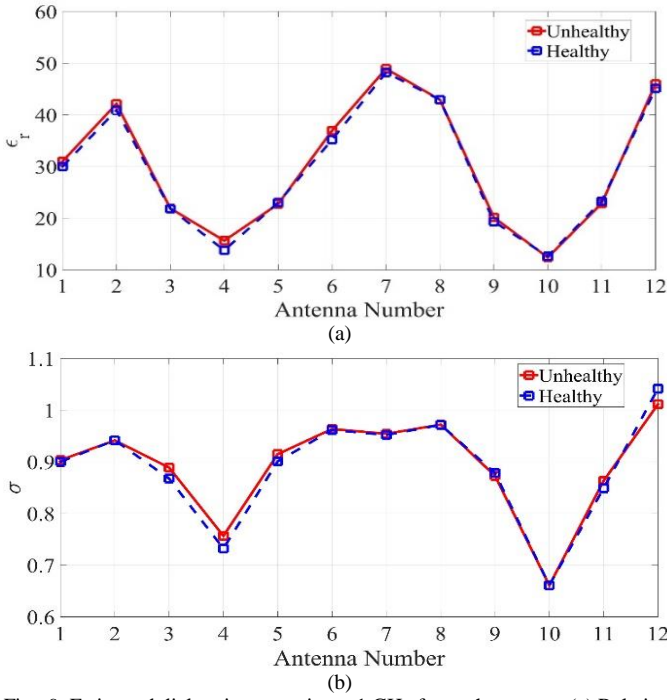


Fig. 9. Estimated dielectric properties at 1 GHz for each antenna. (a) Relative permittivity, and (b) conductivity.

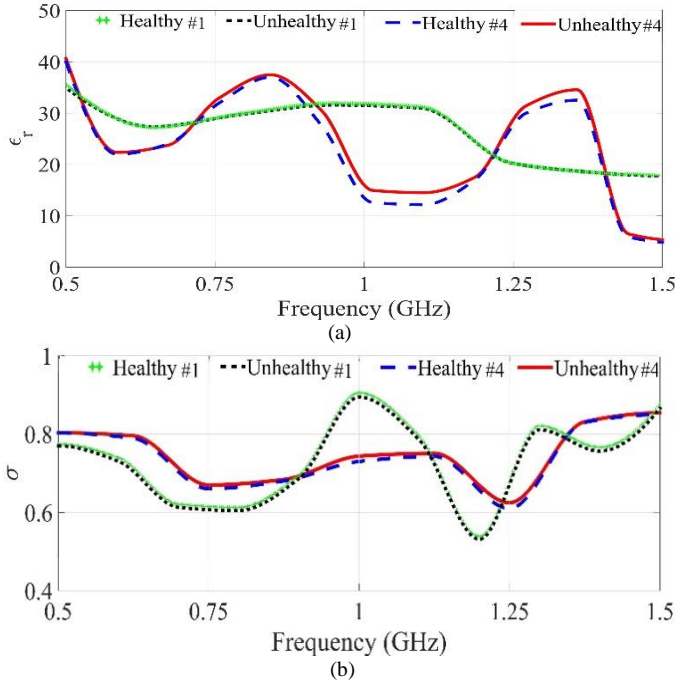


Fig. 10. Estimated dielectric properties for antenna 1 and 4 over the used frequency band. (a) Relative permittivity, and (b) conductivity.

Since the torso includes many types of tissues with frequency dispersive properties, the estimated permittivity fluctuates over the investigated frequency band. The overall trend of the estimated relative permittivity of the torso indicates a decrease in value with frequency. This trend of variation follows the average trend of variation for the permittivity and conductivity of individual tissues as shown in Fig. 7 (b). The average values of the estimated relative permittivity and conductivity over all of the antennas and frequencies are $[\epsilon_r, \sigma] = [29.78, 0.90]$ and $[30.96, 0.91]$, respectively. It's worth noting that these values

are the estimated permittivity of the whole imaging area, including the effect of the air gap between the antennas and the torso.

To investigate the efficacy of the proposed method in the image reconstruction procedure, a frequency-based multistatic microwave imaging algorithm [8] is utilized to process the recorded data and create two-dimensional images. In this algorithm, a modified hybrid clutter removal technique [13], which combines the average subtraction and entropy-based filtering methods is applied to the raw signals:

$$S(i, j; f) = \begin{cases} S_{avg}^*(f) & e^{H_3(f)} \geq N_a^2/2 \\ S_{meas}(i, j; f) & otherwise \end{cases}, \quad (9)$$

where $S_{meas}(i, j; f)$ is the measured signal at i th antenna, transmitted by j -th antenna at frequency f , and S_{avg}^* is the average value of the signals that passes from the third-order Renyi entropy filter:

$$H_3(f) = -\frac{1}{2} \log(\sum_{j=1}^{N_a} \sum_{i=1}^{N_a} [P(i, j; f)]^3) \quad (10)$$

where

$$P(i, j; f) = \frac{\beta(i, j; f) [S_{meas}(i, j; f) - S_{avg}(f)]^2}{\sum_{m=1}^{N_a} \sum_{n=1}^{N_a} w(n, m; f) [S_{meas}(n, m; f) e^{ikr} - S_{avg}(f)]^2}, \quad (11)$$

The weight β adjusts the probability of the calibrated signals according to the corresponding wavenumber of receivers k_i :

$$\beta(i, j; f) = e^{-ik_i/|r_i - r_j|} \quad (12)$$

The clutter removal mitigates the effect of the clutter at all frequencies by applying the average subtraction in every frequency step and then using a modified entropy-based filter to remove the strong reflections from the outer layers (skin and muscle).

After removing the strong reflections, the estimated permittivity values and the recorded signals are used by the imaging algorithm to show the distribution of power intensity inside the imaged region. The purpose of this technique is to image a slice of the three-dimensional torso facing the antennas' ports. Therefore, the imaging region is segmented into 1 mm pixels and the power intensity at each pixel location (x, y) is calculated by superposition of scattering powers produced by different transmitters across the utilized frequency steps ($f_k = 1$ to N_f) [8],

$$I(x, y) = \frac{1}{N_a^2} \left| \sum_{f=1}^{N_f} \sum_{j=1}^{N_a} \sum_{i=1}^{N_a} S(i, j, f) J_1^2(k_i r) e^{-i2k_i r} \right| \quad (13)$$

where S is the measured signal, $J_1(k_i r)$ is the Bessel function, $k_i = 2\pi f(\epsilon_i \mu)^{1/2}$ is the wavenumber and r is the distance from receiver to the pixel. In this equation, a pre-known average permittivity value is usually used to calculate the wavenumber. While, in this work, the estimated permittivity values from (7) which are specific to each antenna and each frequency step, are used to calculate the wavenumber. The reconstructed image can illustrate the location of tumor which has higher dielectric properties than the healthy tissues of the torso.

Fig. 11 shows the reconstructed images using the traditional (one average value) and proposed antenna-specific permittivity

estimation methods for two different locations. The considered average permittivity values in the traditional method (Fig. 11 (a) and (b)) are selected based on the best image quality technique. In this approach, the imaging domain is assumed to have different average dielectric constant values. The signal-to-noise ratio (*SNR*) metric of the obtained images from different assumed dielectric properties are then calculated by

$$SNR = 10 \log_{10} \left(\frac{I_t - I_b}{C_b} \right) \quad (14)$$

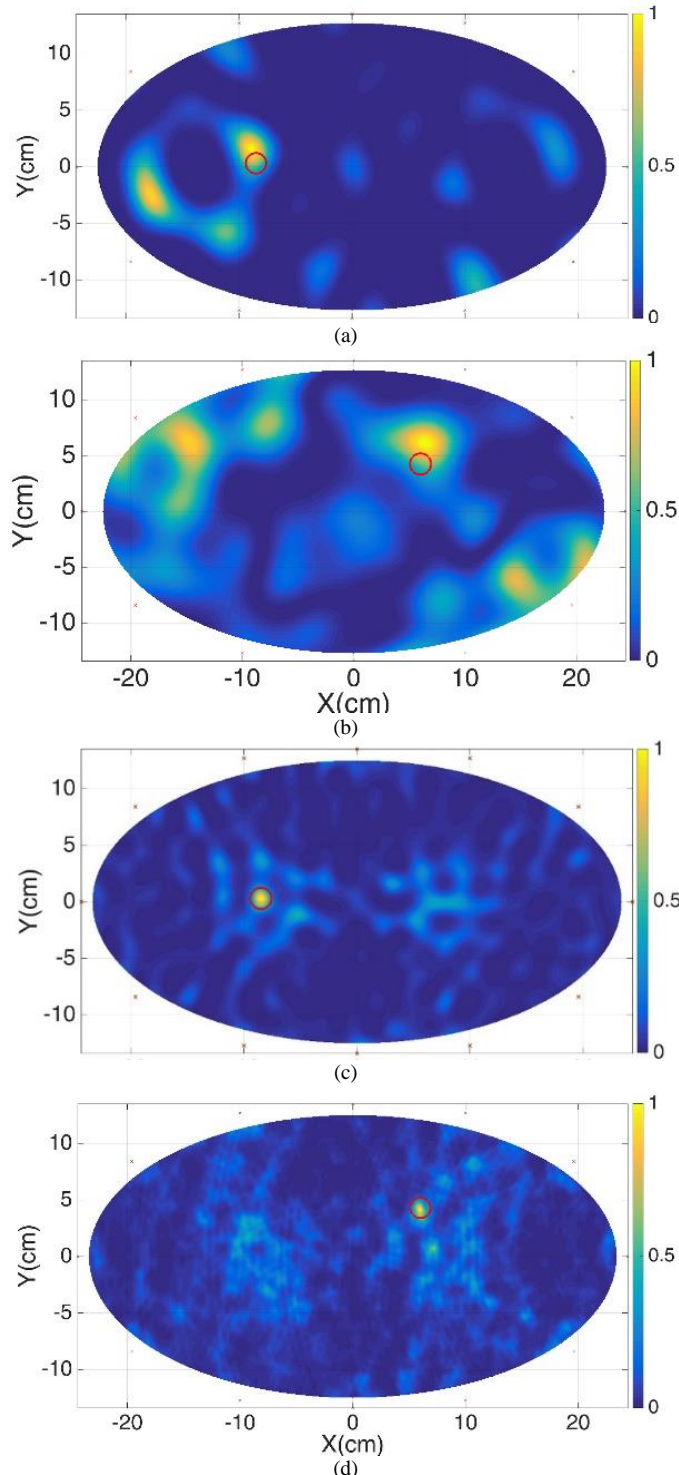


Fig. 11. Reconstructed images (a), (b) before, and (c), (d) after permittivity estimation.

where I_t and I_b are the mean values of the detected target and background regions, respectively, and C_b is the standard deviation of the background. *SNR* reflects the contrast between the target and background. Higher value of *SNR* means higher image quality. Therefore, relevant dielectric properties of the image with the maximum *SNR* value are selected as the dielectric properties of the imaging domain. The obtained average permittivity values from the traditional method are $[\epsilon_r, \sigma] = [23, 0.8]$.

According to Fig. 11, the proposed method can successfully improve the image quality and detection accuracy. It is clear from Fig. 11 (a) and (b) that even using one overall average permittivity value can cause wrong detections by producing false and ghost targets. This happens due to the multipath phenomena occurred in the inhomogeneous torso. On the other hand, Fig. 11 (c) and (d) illustrate that applying the estimated permittivity values to the imaging algorithm provides more accurate detections than the conventional method (Fig. 11 (a) and (b)). In addition, since the estimation of the permittivity is done from the antenna's point of view, the non-uniform distance between the antennas and the torso does not affect the detection accuracy. Moreover, the distribution of the lung tissues with high permittivity values are also roughly revealed in those images. This achievement can lead to more reliable diagnosis of lung cancer and/or other relevant diseases. Although, the exact boundaries of lungs are not clearly displayed in the image, the image quality can be improved by increasing the number of training samples, however, at the expense of computational time and memory. It should be noted that strong reflections of the outer layers, including the skin and muscle tissues, are mitigated in the first step of the imaging algorithm by (9). Hence, those tissues are not shown in the reconstructed images.

To investigate the quality and accuracy of the obtained images, *SNR* and the detection error (Δ) metrics [13] are calculated to quantify the images:

$$\Delta = \|p^* - \alpha\| \quad (15)$$

where α is the real center and p^* represents the center of the detected target. The location of the maximum value of the image is determined as the center of the detected target. Lower Δ means more accurate detection.

Knowing the assumed target size and locations, the metrics are calculated for the reconstructed images in Fig. 11, and listed in Table II. The higher value of *SNR* and lower value of Δ for the images generated using the proposed method compared to the average permittivity method, demonstrate superiority of the proposed method.

TABLE II
IMAGE QUALITY USING CONVENTIONAL AND PROPOSED METHODS

Method	<i>SNR</i> (dB)	Δ (mm)	Figure
Average value	7.01	13.12	Fig. 11 (a)
Average value	3.34	19.90	Fig. 11 (b)
Proposed	12.08	0.00	Fig. 11 (c)
Proposed	11.50	1.12	Fig. 11 (d)

B. Experiments

In order to validate the performance of the proposed method in realistic environments, experiments were performed using an integrated microwave torso imaging system. Fig. 12 shows the configuration of the system. The data acquisition system contains a wall-mounted tube that encloses the subject under test. Twelve antennas are assembled inside the outer layer of the system to form a circular shape multistatic antenna array. The inner cavity is designed in an elliptical shape to form similar structure to that of the human torso. The outer layer of the system is built using expanded Polyvinyl chloride (PVC) with properties that are radiofrequency (RF) transparent, and therefore, it does not affect the radiation performances of the antennas. The antennas are connected to a Keysight L4491A microwave switching system to scan the circumference of the torso. The switching network is connected to the ports of a Keysight N9923A FieldFox vector network analyzer (VNA). The VNA generates the required microwave signal and measures the frequency response of the connected antenna between 0.65 and 1.75 GHz. The VNA and the switches are controlled by a laptop connected via Ethernet and USB connections. A torso phantom comprised of lungs, heart and abdomen block in addition to complete thorax ribs and muscle tissues is utilized (See Fig. 12 (b)). A 1 cm radius sphere built from materials that mimic the dielectric properties of tumor is inserted inside the phantom's lung to imitate a lung cancer scenario.

To analyze the performance of the proposed method, the target is positioned inside the phantom's lung. The phantom is then scanned and the collected data are used to estimate the permittivity of the imaging domain and construct an image of the phantom. Due to the complexity of the experiments and the huge number of required materials, the simulation-based training algorithm is used to estimate the permittivity values in experiments. To that end, the measured signals are calibrated by shifting the signals' frequency and then multiplying them by the calibration factor a :

$$S_{cal}(f) = aS_{exp}(f - f_0) \quad (16)$$

where, S_{cal} is the calibrated signal at frequency f , S_{exp} is the measured signal of experiment, f_0 is the frequency shift which is needed to calibrate the data against the variations in the resonant frequency of the simulated and measured S-parameters. The calibration factor a is calculated for a free space scenario, i.e. by dividing the shifted signals of measurement at free space (without phantom) $S_{exp}^{free}(f - f_0)$ by the simulation signals at free space $S_{sim}^{free}(f)$:

$$a = \frac{S_{exp}^{free}(f - f_0)}{S_{sim}^{free}(f)} \quad (17)$$

The calibrated signals are then used to estimate the dielectric permittivity values and create the final image.

The reconstructed image is shown in Fig. 13, where the small target is exactly detected in the imaging domain. The approximate distribution of the lungs tissues around the target can also be seen in this image.

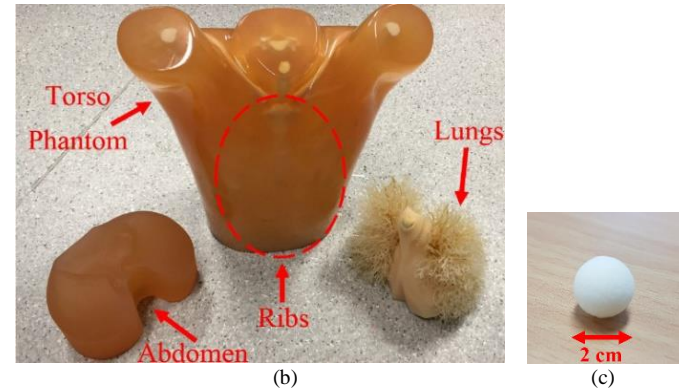


Fig. 12. (a) Torso scanner opened to show its structure and then enclosing a torso phantom, (b) the utilized torso phantom with its inner organs, and (c) the tumor.

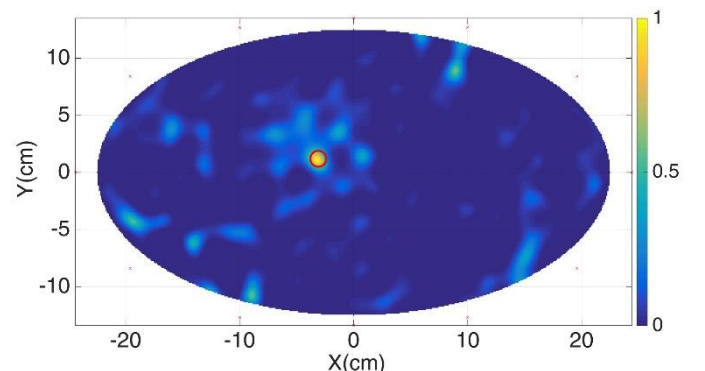


Fig. 13. Resultant image from experiment.

IV. CONCLUSION

A technique for an accurate estimation of the frequency dispersive complex permittivity of an imaging domain has been presented. The aim of the work is to improve the detection and imaging accuracy of multistatic microwave medical imaging systems. To that end, the complex permittivity from the view point of each element is estimated to enhance the image quality. In the proposed technique, the recorded S-parameters are firstly spatially regionalized, and then a spatial statistical model of the dielectric permittivity is produced using a set of training media. The obtained model is used to estimate the frequency dispersive complex permittivity of the imaging domain from the view point of each antenna. The estimated permittivity values are then used as a priori information in a multistatic frequency-based microwave imaging algorithm. The performance of the proposed method was tested using realistic-model simulations and experimentally verified in a torso imaging system where a lung tumor was successfully detected in a torso phantom. The comparison between the constructed images using the proposed and conventional methods shows superiority of the proposed method. In addition, by using the proposed method, there is no need to adjust the distance between the antennas and the imaged object to be uniform or even known as a priori information. This feature is quite important in clinical use of the imaging systems, where the imaged object can be located anywhere inside the imaging domain.

REFERENCES

- [1] P. Meaney, M. Fanning, D. Li, S. Poplack, and K. Paulsen, "A clinical prototype for active microwave imaging of the breast," in *IEEE Trans. Microw. Theory Techn.*, vol. 48, no. 11, pp. 1841–1853, 2000.
- [2] E. J. Bond, Xu Li, S. C. Hagness and B. D. Van Veen, "Microwave imaging via space-time beamforming for early detection of breast cancer," in *IEEE Trans. Antennas Propag.*, vol. 51, no. 8, pp. 1690-1705, 2003.
- [3] D. Byrne, M. Sarafianou, I. Craddock, "Compound Radar Approach for Breast Imaging," in *IEEE Trans. Biomed. Eng.*, vol. PP, no. 99, pp.1-1, 2016.
- [4] E. C. Fear, J. Bourqui, C. Curtis, D. Mew, B. Docktor and C. Romano, "Microwave Breast Imaging with a Monostatic Radar-Based System: A Study of Application to Patients," in *IEEE Trans. Microw. Theory Techn.*, vol. 61, no. 5, pp. 2119-2128, May 2013.
- [5] R. K. Amineh, M. Ravan, A. Khalatpour and N. K. Nikolova, "Three-Dimensional Near-Field Microwave Holography Using Reflected and Transmitted Signals," in *IEEE Trans. Antennas Propag.*, vol. 59, no. 12, pp. 4777-4789, Dec. 2011.
- [6] S. Caorsi, A. Massa, M. Pastorino and M. Donelli, "Improved microwave imaging procedure for nondestructive evaluations of two-dimensional structures," in *IEEE Trans. Antennas Propag.*, vol. 52, no. 6, pp. 1386-1397, June 2004.
- [7] A. Zamani, S.A. Rezaeieh, and A.M. Abbosh, "Lung cancer detection using frequency-domain microwave imaging," *Electronics Letters*, vol. 51, no. 10, pp. 740-741, 2015.
- [8] A. Zamani, A. M. Abbosh and A. T. Mobashsher, "Fast Frequency-Based Multistatic Microwave Imaging Algorithm with Application to Brain Injury Detection," in *IEEE Trans. Microw. Theory Techn.*, vol. 64, no. 2, pp. 653-662, Feb. 2016.
- [9] K. K. M. Chan, A. E. C. Tan, L. Li, and K. Rambabu, "Material Characterization of Arbitrarily Shaped Dielectrics Based on Reflected Pulse Characteristics," *IEEE Trans. Microw. Theory Techn.*, vol. 63, no. 5, pp. 1700-1709, May, 2015.
- [10] J. Bourqui and E. C. Fear, "System for Bulk Dielectric Permittivity Estimation of Breast Tissues at Microwave Frequencies," *IEEE Trans. Microwave Theory Techn.*, vol. 64, pp. 3001-3009, 2016.
- [11] D. W. Winters, E. J. Bond, B. D. Van Veen and S. C. Hagness, "Estimation of the Frequency-Dependent Average Dielectric Properties of Breast Tissue Using a Time-Domain Inverse Scattering Technique," in *IEEE Trans. Antennas Propag.*, vol. 54, no. 11, pp. 3517-3528, Nov. 2006.
- [12] M. Sarafianou *et al.*, "MUSIC processing for permittivity estimation in a Delay-and-Sum imaging system," *2013 7th European Conference on Antennas and Propagation (EuCAP)*, Gothenburg, 2013, pp. 839-842.
- [13] A. Zamani and A. Abbosh, "Hybrid Clutter Rejection Technique for Improved Microwave Head Imaging," in *IEEE Trans. Antennas Propag.*, vol. 63, no. 11, pp. 4921-4931, Nov. 2015.
- [14] B. J. Mohammed, K. S. Bialkowski and A. M. Abbosh, "Radar-based time-domain head imaging using database of effective dielectric constant," in *Electronics Letters*, vol. 51, no. 20, pp. 1574-1576, 10 1 2015.
- [15] L. Guo and A. M. Abbosh, "Optimization-Based Confocal Microwave Imaging in Medical Applications," in *IEEE Trans. Antennas Propag.*, vol. 63, no. 8, pp. 3531-3539, Aug. 2015.
- [16] B. Lavoie, M. Okoniewski, E. Fear, "Estimating the Effective Permittivity for Reconstructing Accurate Microwave-Radar Images," *PLoS ONE*, vol. 11, no. 9, 2016.
- [17] S. Salman, D. Psychoudakis and J. L. Volakis, "Determining the Relative Permittivity of Deep Embedded Biological Tissues," in *IEEE Antennas Wireless Propag. Lett.*, vol. 11, pp. 1694-1697, 2012.
- [18] M. A. Islam, A. Kiourti and J. L. Volakis, "A Novel Method of Deep Tissue Biomedical Imaging Using a Wearable Sensor," in *IEEE Sensors J.*, vol. 16, no. 1, pp. 265-270, Jan.1, 2016.
- [19] N. Cressie, "Statistics for Spatial Data," in *Statistics for Spatial Data, Revised Edition*, Hoboken: Wiley, 1993.
- [20] A. C. Aitken, "On Least-squares and Linear Combinations of Observations," presented in *Proceedings of the Royal Society of Edinburgh*, no. 55, pp. 42–48. 1934.
- [21] A. Papritz, A. Stein, "Spatial prediction by linear kriging", in *Spatial Statistics for Remote Sensing*, vol. 1, A. Stein, F. Van Der Meer and B. Gorte Ed. Dordrecht, Netherlands: Springer, 2002, pp. 83-113.
- [22] C. K. I. Williams, "Prediction with Gaussian Processes: From Linear Regression to Linear Prediction and Beyond," in *Learning in Graphical Models*, vol. 89, M.I. Jordan, Ed. Dordrecht, Netherlands: Springer, 1998, pp. 599–621.
- [23] L. Tsang, K. H. Ding, S. Huang and X. Xu, "Electromagnetic Computation in Scattering of Electromagnetic Waves by Random Rough Surface and Dense Media in Microwave Remote Sensing of Land Surfaces," in *Proc. IEEE*, vol. 101, no. 2, pp. 255-279, Feb. 2013.
- [24] J. P. C. Kleijnen, "Kriging Metamodeling in Simulation: A Review," *European Journal of Operation Research*, vol. 192, no. 3, pp. 707-716, 2009.
- [25] S. A. Rezaeieh, A. Zamani, K. S. Bialkowski, and A. M. Abbosh, "Novel Microwave Torso Scanner for Thoracic Fluid Accumulation Diagnosis and Monitoring," *Nature, Scientific Reports*, March 2017.
- [26] O. M. Bucci, and T. Isernia, "Electromagnetic inverse scattering: Retrievable information and measurement strategies," *Radio Science*, vol. 32, no. 6, pp. 2123-2137, Nov-Dec, 1997.
- [27] V. Clemson, Y. Tang, J. Pyne, and R. Unal, "Efficient methods for sensitivity analysis," *System Dynamics Review*, no. 11, pp. 31-49, 1995.